

Investigating the Relationship between Water Vapor
Convergence and Severe Convection using the
Weather Research and Forecasting (WRF) Model.

James M Done, Xiang-Yu Huang*and Ying-Hwa Kuo

National Center for Atmospheric Research, US

December 14, 2006

**Corresponding author address:* Xiang-Yu Huang, National Center for Atmospheric Research, P.O. Box 3000, Boulder, CO 80307, USA ; e-mail: huangx@ucar.edu

Abstract

Numerical simulations of severe convection using a grid spacing of 1km and output data every minute are examined to determine the relationship between low-level water vapor convergence and severe convection. For three cases of severe convection each of a different convective mode; a bow-echo system, a leading line MCS and a line of supercells, low-level water vapor convergence is found to evolve two timescales; a slow increase on synoptic/mesoscale timescales in the hours before convection followed by a fast increase close to the onset of severe convection. This rapid increase of water vapor can serve as a useful precursor to severe convection. Precursors are found to exist independent of spatial scale, from the mesoscale down to the smallest resolvable scales of the model (6 - 8km). At spatial scales appropriate for nowcasting applications, approximately 30km, lead times of the precursors fall in the range 20 and 40 minutes and are therefore useful for providing warnings for the possibility of severe weather.

1 Introduction

Nowcasting severe weather remains a challenging problem. Under convectively unstable conditions successful nowcasting largely depends on the ability to predict the timing and location of convective initiation (Stensrud, 2001) . Guidance on convection initiation from Numerical Weather Prediction (NWP) models and nowcasting systems can be poor, largely due to (i) incomplete knowledge concerning the mechanisms of convection initiation and (ii) small scales that can act to trigger convection in nature are often poorly resolved, if included at all, in current NWP models (e.g. Stensrud *et al.*, 1999) . Scientific knowledge is currently being advanced through field campaigns such as the International H2O project (Weckwerth and Coauthors, 2004) and the improvement of numerical guidance and automated nowcasting systems is an active area of research (see for example Wilson *et al.*, 2004) . Despite continuing advancements, the role of diagnostic aids in nowcasting remains important to the success of severe weather nowcasting (Banacos and Schultz, 2005) .

Severe convection is often preceded by an increase in low-level water vapor convergence, as discussed in Banacos and Schultz (2005). It follows that observations of low-level water vapor convergence can potentially increase the lead-time and knowledge of locations for nowcasting severe weather. Indeed, surface observations of moisture convergence have been widely applied in nowcasting the locations of convective initiation. An increase in low-level water vapor convergence might be observed in the hours before the onset of severe convection. However, the area covered by the water vapor convergence might be large, so the precise location of severe convection would not be detectable. It is plausible that closer to the onset of severe convection an area with an increased signal in water vapor convergence could be observed, which would give lead-time for a warning over a specific area.

In this study, output from high-resolution numerical simulations of severe convection case studies are examined to determine the relationship between water vapor convergence and severe convection. Using a grid spacing of 1km and output data every minute, the pre-convective evolution of the water vapor field is examined in an attempt to identify and characterize behaviour that may be useful for nowcasting the timing and location of convection initiation and severe weather. The state-of-the-art Weather Research and Forecasting (WRF) model (Michalakes *et al.*, 2001) is used to simulate three cases of severe convection.

Brief descriptions of the cases studies of severe convection are provided in section 2, followed by an overview of the numerical modeling system in section 3. Analysis of numerical simulations are presented in sections 4 and 5. Finally, results are summarized and recommendations are given in section 6.

2 Case Studies

Cases of severe convection are selected from the period of the the Bow-Echo and Mesoscale Convective Vortex Experiment (BAMEX; Davis *et al.* (2004)). The overarching strategy of BAMEX was to observe the lifecycle of Mesoscale Convective Systems (MCSs), through their organisation, maturation, dissipation and ultimate downstream regeneration. Operations were conducted between mid-May and early July 2003 over the Midwest United States. Extensive observational data of the cases, including radar and satellite animations, are archived at <http://catalog.eol.ucar.edu/bamex/>.

The relationship between water vapor convergence and severe convection may depend on the convective environment and convective-system mode. Therefore, in an attempt to provide a set of cases representing a cross-section of convective environments, three

cases are selected, each of different convective-system mode.

Case 1 is the severe bow-echo system¹ observed during 9-10 June 2003. Two tornadic supercells formed over northeast Nebraska around 0000 UTC 10 June ahead of an upper-level wave. Two distinct bow structures quickly developed and subsequently consolidated into a continuous line that assumed a storm motion of 17ms^{-1} towards the southeast (128°). The mature bow-echo system is shown in the right panel of Fig. 1. The complete lifecycle of the system took place within a 24 hour period.

The convective system in Case 2 is characterized by a leading line of convective cells and a trailing stratiform region, known as a leading-line MCS. Convection was triggered over Oklahoma and Kansas from 2100 UTC 10 June along a trailing cold front. Whereas the convective environment of case 1 was characterized by weak thermodynamic gradients at low levels, convection for this case was initiated along the strong thermodynamic gradient of the cold front. Convection subsequently organized overnight into a leading-line MCS, shown in the right panel of Fig. 2.

Case 3 is a line of supercells that tracked across the Great Lakes region on 30th May 2003. An upper-level shortwave trough moved southeastward into the Great Lakes region, and convection was initiated under strong forcing along a trailing cold front south of a surface low. Although instability was weak to moderate, strong shear of the horizontal wind supported supercells. The line of supercells is shown in the right panel of Fig. 3.

¹See Fujita (1978) and Weisman (2001) for a description of bow-echo systems.

3 The Weather Research and Forecasting (WRF) model

The WRF model (Michalakes *et al.*, 2001) is an advanced mesoscale and data assimilation system designed for cloud and mesoscale (1-10km) applications over a limited area. The model uses an Eulerian solver based on a flux formulation to solve the fully compressible non-hydrostatic equations that govern the dynamics and thermodynamics of the atmospheric circulation. The Eulerian solver uses a third order Runge-Kutta time integration, third to fifth order advection operators, and split-explicit acoustic/gravity wave integration (Wicker and Skamarock, 2002) conserving both mass and energy. The high-order numerical methods make the WRF model well suited for the high resolution simulations proposed in this study. In addition, a suite of physics options have been designed specifically for high resolution applications and have been rigorously tested for convective situations (Done *et al.*, 2004) .

BAMEX provided an unprecedented opportunity to evaluate many WRF model forecasts of severe convection. During the field phase of BAMEX, 36hr real-time forecasts were conducted daily with version 1.3 of WRF using a 4km horizontal grid-spacing over the central United States. Details of the selected physics parameterizations are given in Done *et al.* (2004). A grid-spacing of 4km is considered sufficient to represent MCSs explicitly without the need for a parameterization of convection (Weisman *et al.*, 1997) but is still insufficient for representing many cell-scale processes critical for severe weather forecasting, as discussed in Bryan *et al.* (2003). Done *et al.* (2004) showed these explicit convection forecasts were able to accurately predict the number of MCSs daily, the convective-system mode and evolution of the MCSs. Examples of useful WRF forecasts are shown for the three selected cases in the left panels of Figs.

1, 2 and 3 together with observations shown in the right panels. WRF forecasts during BAMEX are archived at <http://www.joss.ucar.edu/bamex/catalog>.

3.1 Model Setup

The model setup is similar to that of the real-time BAMEX WRF forecasts. The model version current as of October 2004 (version 2.0.3) is used with one-way nesting down to 1km grid-spacing. All domains have 35 terrain-following levels specified in the vertical, spaced roughly 250m apart in the lowest km with monotonic stretching to about 1km spacing near and above 14km. The model top is at 50hPa. The basic physics packages are the same for both domains and include the Mellor-Yamada-Janjic (ETA) boundary layer scheme, the Noah land surface model, and the Lin microphysics scheme with 6 prognostic moisture variables (derived from the original scheme described in Lin *et al.* (1983)). Second-order diffusion is applied in the horizontal, and damping is applied to vertical velocity. Convective parameterization is not used and no additional data are assimilated.

The parent domain used for all simulations is shown in Fig. 4 together with the nested domains for each of the three case studies. The parent domain of 500×500 grid points uses 4km horizontal grid-spacing. Initial and boundary conditions are derived from the 40km ETA analyses available at 3 hourly intervals. Boundary conditions at each timestep are interpolated between the 3 hourly ETA analyses. The parent domain communicates with the nested domain by providing boundary conditions at each timestep. Nested domains of approximately 600×500 grid points use 1km horizontal grid-spacing, and are located such that convection initiates close to the center of the domain. Both parent and nested domains are initialized using the ETA analyses, approximately six hours prior to the observed initiation of convection. Simulations run for

12 hours and capture the pre-convective environment, convection initiation and subsequent mesoscale convective organization. This allows for study of the evolution of the water vapor field prior to convection and to determine the relationship between water vapor convergence and severe convection. Data from the nested domain are archived every minute.

4 Analysis of Case 1: Bow-Echo

The simulation of case 1 captured the approximate timing and location of the observed convection initiation, close to the center of the nested domain at approximately 0130 UTC 10 June 2003. Model convection quickly organized into a propagating bow-echo system, as observed. Further convection initiated within the nested domain and subsequently merged with the bow-echo system, as observed. The simulation is therefore adequate to investigate the relationship between water vapor convergence and severe convection. A sub-region of the nested domain of dimensions $151\text{km} \times 151\text{km}$ is used later to calculate area averaged quantities and to isolate the water vapor signature associated with the bow-echo system. The sub-region includes the pre-convective environment, initiation and organisation of the bow-echo and is shown in Fig. 4.

4.1 Relationship with Water Vapor Convergence

Following Kuo (1974), low-level water vapor convergence is defined as;

$$-\int \rho \nabla \cdot (q\mathbf{V}_h) dZ, \quad (1)$$

where ρ is density, q is water vapor mixing ratio, \mathbf{V}_h is the 2-dimensional wind field and Z is geopotential height. Low-level is defined here as the depth of the boundary layer of the convective environment taken from observed thermodynamic profiles.

Remote sensing methods often observe total column water vapor, known as Precipitable Water (PW) and assume the time tendency of PW provides an estimate for low-level water vapor convergence.

PW is defined as;

$$\int \rho q dZ. \quad (2)$$

Therefore, the time rate of change of total column water vapor can be expressed as;

$$\frac{\partial PW}{\partial t} = \int \rho \frac{\partial q}{\partial t} dZ. \quad (3)$$

We know that;

$$\frac{\partial q}{\partial t} + \mathbf{V} \cdot \nabla q = Q, \quad (4)$$

where \mathbf{V} is the 3d wind field and Q represents the sources and sinks of water vapor mixing ratio. Rearranging Eqn. 4 for $\frac{\partial q}{\partial t}$ and combining with Eqn 3 gives;

$$\frac{\partial PW}{\partial t} = \int \rho Q dZ - \int \rho \mathbf{V} \cdot \nabla q dZ, \quad (5)$$

and it follows that;

$$\frac{\partial PW}{\partial t} = \int \rho Q dZ - \int \rho \nabla \cdot \mathbf{V} q dZ + \int \rho q \nabla \cdot \mathbf{V} dZ. \quad (6)$$

The time rate of change of PW therefore depends on the source/sink terms, the vertically integrated 3d water vapor convergence and a 3d mass convergence term. The time rate of change of PW and vertically integrated water vapor convergence are therefore not the same quantity and may have different relationships with severe convection.

A model vertical profile ahead of the propagating bow-echo and a vertical profile obtained from a dropsonde in the same location (not shown) both show the top of the boundary layer at approximately 800mb. Low-level (dZ) is therefore defined as the surface to 800mb layer.

Figure 5a shows a timeseries of low-level water vapor convergence and 1 minute accumulated rainfall, averaged over the sub-region. 1-minute rainfall amount is used here as a proxy for convection. Water vapor convergence appears to evolve on two timescales; a slow increase in the hours before convection followed by a fast increase close to the onset of convection. This suggests mechanisms are operating on two timescales; the slow increase associated with the synoptic/mesoscale development of the convective environment and the fast increase associated with a precursor mechanism to convection. This suggests a relationship between low-level water vapor convergence and severe convection.

Figure 5b shows timeseries of the time rate of change of PW using $\Delta t = 1$ minute and 1 minute accumulated rainfall, both averaged over the sub-region. As for low-level water vapor convergence, $\Delta PW / \Delta t$ evolves on two timescales; a slow increase on

synoptic/mesoscale timescales in the hours before convection followed by a fast increase close to the onset of severe convection. This suggests a relationship between $\Delta PW/\Delta t$ and severe convection.

4.2 Lead-Times of the Precursors to Severe Convection

Precursors to severe convection have been identified in the time-series of low-level water vapor convergence and $\Delta PW/\Delta t$. Knowledge of the lead-time of the precursor is useful for nowcasting purposes. An estimate for the lead-times can be obtained by correlating the 1-minute rainfall field with either the water vapor convergence field or the $\Delta PW/\Delta t$ field. Ratio Y is calculated as follows;

$$Y(t) = \frac{R(n)}{W(n-t)}, \quad (7)$$

where R is the number of grid points exceeding a 1-minute rain amount threshold (R_c) at the time of the onset of severe convection n . For this case, $n = 560$ minutes into the simulation. W is the number of those grid points that exceed a low-level water vapor convergence threshold (WV_c) at different lead times t . To obtain the ratio for $\Delta PW/\Delta t$, the low-level water vapor convergence field is substituted for the $\Delta PW/\Delta t$ field. In converting the fields to binary, dependence on the magnitude is removed, and the ratio becomes a measure of overlap between shapes in the rainfall and water vapor convergence or $\Delta PW/\Delta t$ fields.

Figure 6a shows the ratio Y as a function of lead-time, t , for different values of the tunable threshold parameters R_c and WV_c . The shape of the timeseries are not sensitive to the threshold parameters, and maximum ratios occur around 30 minutes lead-time for

low-level water vapor convergence. Figure 6b shows the maximum ratios for $\Delta PW / \Delta t$ occur around 40 minutes. This result compares well with the observational study of Seko *et al.* (2004) that showed increases in water vapor 20 minutes prior to convective precipitation cores.

4.3 Sensitivity to Averaging Area

A precursor to severe convection has been identified in low-level water vapor convergence on the scale of the sub-region averaging area ($151\text{km} \times 151\text{km}$). For nowcasting purposes it is desirable to detect precursors over smaller spatial scales to be more precise on the location for severe weather warnings. Here, the sensitivity of characteristics of the precursor to the size of the averaging area are examined.

Figure ?? shows timeseries of area averaged low-level water vapor convergence and 1 minute accumulated rainfall for three averaging areas; $151\text{km} \times 151\text{km}$, $75\text{km} \times 75\text{km}$ and $31\text{km} \times 31\text{km}$. The center grid-point for all averaging areas is the same, resulting in box lengths of uneven number of grid spacings. A precursor is present for all averaging area sizes, and the time of the peak magnitude in water vapor convergence has low sensitivity to the averaging area size. Since the center point lies approximately at the location of highest rainfall amount, it follows that the magnitude of the area-averaged quantities increases as the averaging area is reduced. Similar results are found for the precursor in $\Delta PW / \Delta t$ (not shown).

For averaging areas less than $31\text{km} \times 31\text{km}$, the timeseries of area-averaged water vapor convergence and rainfall become 'noisy' with multiple maxima for an averaging area of $11\text{km} \times 11\text{km}$ (not shown). It becomes unclear whether this is realistic small-scale variability associated with individual convective cells or numerical noise. Skamarock

(2004) showed that scales of 6 to 8 times the grid-spacing are handled well in NWP models. This suggests that information on scales greater than, say, 8km is realistic, and that precursors exist in the water vapor convergence even at these smaller scales. The change from single maxima to multiple maxima in the timeseries of water vapor convergence and rainfall as the averaging area is reduced may be due to the change from mesoscale behaviour to the behaviour of individual convective cells. Lead times of the precursors are less at these smaller scales. Information on scales greater than 31km is perhaps sufficient for nowcasting severe convection since the counties in regions of the US prone to severe weather are often on a much larger scale.

4.4 Sensitivity to Temporal Resolution

To determine the sampling frequency of low-level water vapor convergence necessary to capture the precursor for nowcasting severe weather, the sensitivity of the precursor in low-level water vapor convergence to the temporal resolution of the data is examined.

Figure 7 shows there are no significant differences in the timeseries of area average water vapor convergence using different temporal resolution data in the range 1 min to 30 min for an averaging area of 31km \times 31km. The magnitude and 'shape' of the precursor at a spatial scale of 31km therefore has low sensitivity to the temporal resolution of the data. As expected, this result is independent of the averaging area size for square boxes with side lengths between 31km and 151km (not shown). Similar results are found for the precursor in $\Delta PW / \Delta t$ (not shown).

Assuming information on scales of 31km is sufficient for future nowcasting applications, then sampling water vapor convergence every 30 minutes is sufficient to capture the precursor to severe convection. However, given a lead-time of 30 minutes, a higher

sampling rate may be useful.

5 Analysis of Case 2: Leading-Line MCS and Case 3: Line of Supercells.

Similar analysis as for case 1 has been performed for cases 2 and 3, and brief overviews are provided here.

Simulations of cases 2 and 3 both captured the approximate location and timing of convection initiation close to the centre of the nested domains, and captured the observed convective mode; a leading line MCS for case 2 and a line of supercells for case 3. The numerical simulation data are therefore adequate to investigate the relationship between water vapor convergence and severe convection.

As for case 1, simulations of cases 2 and 3 show fast increases in area averaged low-level water vapor convergence (shown in Fig. 8) and $\Delta PW / \Delta t$ (not shown) prior to severe convection. Again, these precursors suggest a relationship with severe convection. Using a similar correlation technique as for case 1, maximum correlations between the field of 1-minute rainfall and either water vapor convergence or $\Delta PW / \Delta t$ occur around lead-times of 20 minutes for case 2 and 30 minutes for case 3 (not shown). In addition, characteristics of the precursors, such as the 'shape' and lead-time, have low sensitivity to the size of the averaging area (not shown), and to the temporal resolution of the data in the range 1 min to 30 min (shown in Figs 9 and 10 for box averages of size 31km).

6 Summary

High-resolution numerical simulations of severe convection have been examined using 1-minute output data to determine the relationship between low-level water vapor convergence and severe convection.

For three cases of severe convection each of a different convective mode; a bow-echo system, a leading line MCS and a line of supercells, low-level water vapor convergence evolved on two timescales; a slow increase on synoptic/mesoscale timescales in the hours before convection followed by a fast increase close to the onset of severe convection.

This rapid increase of water vapor convergence can serve as a useful precursor to severe convection. Precursors were found to exist independent of spatial scale, from the mesoscale down to the smallest resolvable scales of the model (6 - 8km). At the larger scales the precursors are associated with the mesoscale evolution of the pre-convective environment whereas at the smallest scales it is thought that the precursors are signatures of individual convective cells. For nowcasting purposes, it is perhaps sufficient to obtain information on spatial scales of, say, 30km and at these scales the precursors have lead-times between 20 and 40 minutes. Lead times in this range are useful for providing warnings for the possibility of severe weather. At spatial scales of 30km, the sampling rate necessary to capture the precursors was found to be 30 minutes or less. However, given typical lead-times of 20 - 40 minutes, a higher sampling rate would be necessary in order to issue timely warning of severe weather.

Information on the lead-time is useful for the design of future observation systems. Indeed, this study was part-motivated by the need to determine the optimal repeat cycle of water vapor observations by EUMETSAT's Meteosat Third Generation (MTG) geostationary satellite, due to commence operations in 2015. Information on the water

vapor field using remote sensing instrumentation is usually derived from observations of PW and the time tendency of PW is often used as a proxy for low-level water vapor convergence. In this study, precursors in the time tendency of PW have similar characteristics to their counterparts in the actual low-level water vapor convergence field, and it is therefore valid to relate apply the results to remote sensing applications. For the MTG application, a sampling rate of 10 minutes has been considered sufficient to identify precursors in the moisture field and issue timely warnings on the possibility of severe weather. The MTG study is summarized by Huang *et al.* (2005) and can be found at <http://www.eumetsat.int/>.

ACKNOWLEDGEMENTS. This study was performed under EUMETSAT contract.
Ref: EUM/PPS/SOW/04/0089

References

- Banacos, P. and Schultz, D. (2005). The use of moisture flux convergence in forecasting convective initiation: Historical and operational perspectives. *Wea. Forecasting.*, **20**, 351–366.
- Bryan, G., Wyngaard, J., and Fritsch, J. (2003). Resolution requirements for the simulation of deep moist convection. *Mon. Wea. Rev.*, **131**, 2394–2416.
- Davis, C., Atkins, N., Bartels, D., Bosart, L., Coniglio, M., Bryan, G., Cotton, W., Dowell, D., Jewett, B., Johns, R., Jorgenson, D., Knievel, J., Knupp, K., Lee, W.-C., McFarquar, G., Moore, J., Pryzbylinski, R., Rauber, R., Smull, B., Trapp, R., Trier, S., Wakimoto, R., Weisman, M., and Ziegler, C. (2004). The Bow-Echo and MCV Experiment (BAMEX): Observations and opportunities. *Bull. Amer. Meteor. Soc.*, **85**, 1075–1093.
- Done, J., Davis, C., and Weisman, M. (2004). The next generation of NWP: Explicit forecasts of convection using the weather research and forecasting (WRF) model. *Atmos. Sci. Letters.*, **5**, 110–117.
- Fujita, T. (1978). Manual of downburst identification for project NIMROD. In *Satellite and Mesometeorology Research Paper*, number 156, page 104. Department of Geophysical Sciences, University of Chicago.
- Huang, X.-Y., Kuo, Y.-H., and Done, J. (2005). Report TN-3: Potential of Meteosat Third Generation to detect water vapor convergence linked to severe convection. Eumetsat Report TN-3.

- Kuo, H.-L. (1974). Further studies of the parameterization of the influence of cumulus convection on the large-scale flow. *J. Atmos. Sci.*, **31**, 1231–1240.
- Lin, Y.-L., Farley, R., and Orville, H. (1983). Bulk parameterisation of the snow field in a cloud model. *J. Clim. Appl. Meteorol.*, **22**, 1065–1092.
- Michalakes, J., Chen, S., Dudhia, J., Hart, L., Klemp, J., Middlecoff, J., and Skamarock, W. (2001). Development of a next generation regional weather research and forecast model. In *Developments in Teracomputing: Proceedings of the Ninth ECMWF Workshop on the Use of High Performance Computing in Meteorology*, Zweiflhofer W, Krietz N(eds)., pages 269–276. World Scientific: Singapore.
- Seko, H., Nakamura, H., Shoji, Y., and Iwabuchi, T. (2004). The meso-gamma scale water vapor distribution associated with a thunderstorm calculated from a dense network of gps receivers. *J. Meteor. Soc. Japan.*, **82**, 569–586.
- Skamarock, W. (2004). Evaluating mesoscale NWP models using kinetic energy spectra. *Mon. Wea. Rev.*, **132**, 3019–3032.
- Stensrud, D. (2001). Using short-range ensemble forecasts for predicting severe weather events. *Atmos. Res.*, **56**, 3–17.
- Stensrud, D., Manikin, G., Rogers, E., and Mitchell, K. (1999). Importance of cold pools to NCEP mesoscale Eta model forecasts. *Wea. Forecasting.*, **14**, 650–670.
- Weckwerth, T. M. and Coauthors (2004). An overview of the International H2O

Project (IHOP-2002) and some preliminary highlights. *Bull. Amer. Meteor. Soc.*, **85**, 253–277.

Weisman, M. (2001). Bow echoes: A tribute to T. T. Fujita. *Bull. Amer. Meteor. Soc.*, **82**, 97–116.

Weisman, M., Skamarock, W., and Klemp, J. (1997). The resolution dependence of explicitly modeled convective systems. *Mon. Wea. Rev.*, **125**, 527–548.

Wicker, L. and Skamarock, W. (2002). Time-splitting methods for elastic models using forward time schemes. *Mon. Wea. Rev.*, **130**, 2088–2097.

Wilson, J., Ebert, E. E., Saxen, T. R., Roberts, R. D., Mueller, C. K., Sleigh, M., Pierce, C. E., and Seed, A. (2004). Sydney 2000 forecast demonstration project: Convective storm nowcasting. *Wea. Forecasting*, **19**, 131–150.

Figure Caption List

1. The bow-echo system at 0800 UTC 10 June shown in (right panel) observed maximum reflectivity in each column (2km grid), and (left panel) WRF model derived maximum reflectivity in each grid column (dBZ) from the BAMEX WRF forecast initialized at 0000 UTC 9 June (4km grid).
2. The leading line MCS at 0600 UTC 11 June shown in (right panel) observed maximum reflectivity in each column (2km grid), and (left panel) WRF model derived maximum reflectivity in each grid column (dBZ) from the BAMEX WRF forecast initialized at 0000 UTC 10 June (4km grid).
3. The line of supercell convection at 2300 UTC 30 May shown in (right panel) observed maximum reflectivity in each column (2km grid), and (left panel) WRF model derived maximum reflectivity in each grid column (dBZ) from the BAMEX WRF forecast initialized at 0000 UTC 30 May (4km grid).
4. The parent domain and nested domains for each of the three case studies. The box inside domain 1 indicates a sub-region of the nested domain used to calculate area average quantities for case 1.
5. (a) Timeseries of 1-minute rainfall accumulation (mm, solid line) and low-level water vapor convergence ($\text{kgm}^{-2}\text{s}^{-1}$, dashed line), and (b) Timeseries of 1-minute rainfall accumulation (mm, solid line) and time rate of change of PW using $\Delta t = 1\text{min}$ ($\text{kgm}^{-2}\text{s}^{-1}$, dashed line). All quantities are area averages taken over the sub-region shown in Fig. 4.
6. Ratio of the number of grid points exceeding a rainfall threshold to the number of those grid point exceeding (a) a water vapor convergence threshold and (b) a $\Delta PW / \Delta t$ threshold, for different thresholds.

7. Timeseries of 1-minute rainfall accumulation (mm, dashed) and low-level water vapor convergence ($\text{kgm}^{-2}\text{s}^{-1}$, solid) averaged over a 31km square box using data of degraded temporal resolution.
8. Timeseries of 1-minute rainfall accumulation (mm, solid line) and low-level water vapor convergence ($\text{kgm}^{-2}\text{s}^{-1}$, dashed line) averaged over a 151km square box for (left panel) case 2 and (right panel) case 3.
9. As for Fig. 7 but for case 2.
10. As for Fig. 7 but for case 3.

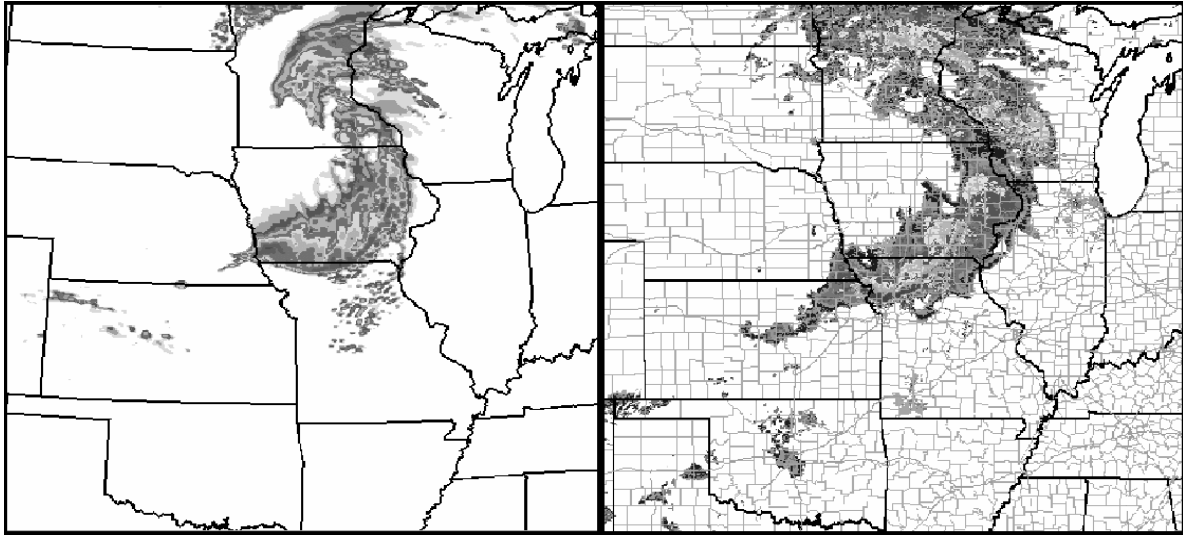


Figure 1: The bow-echo system at 0800 UTC 10 June shown in (right panel) observed maximum reflectivity in each column (2km grid), and (left panel) WRF model derived maximum reflectivity in each grid column (dBZ) from the BAMEX WRF forecast initialized at 0000 UTC 9 June (4km grid).

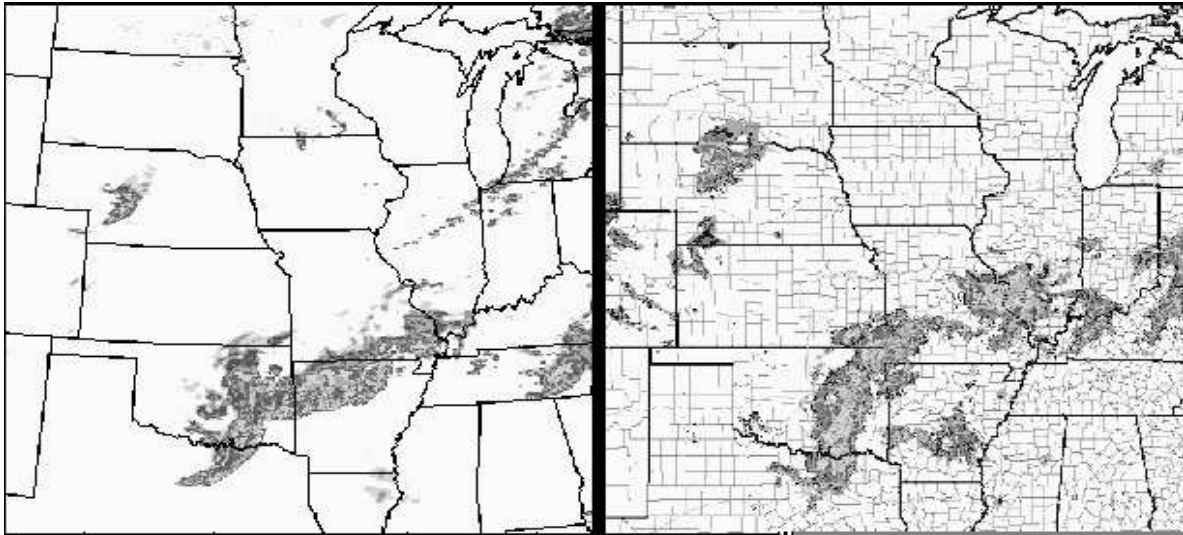


Figure 2: The leading line MCS at 0600 UTC 11 June shown in (right panel) observed maximum reflectivity in each column (2km grid), and (left panel) WRF model derived maximum reflectivity in each grid column (dBZ) from the BAMEX WRF forecast initialized at 0000 UTC 10 June (4km grid).

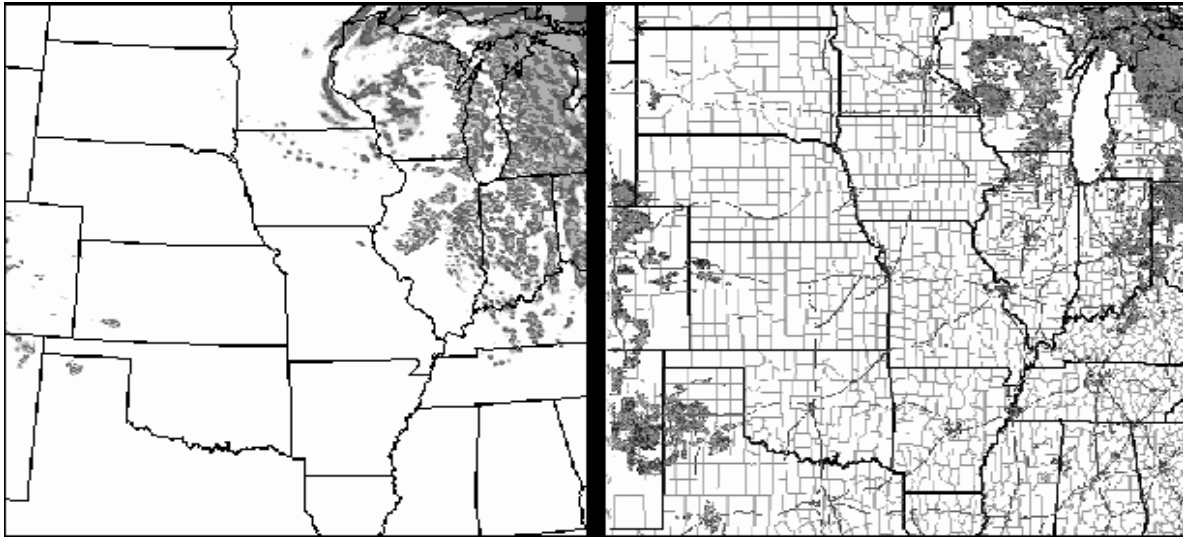


Figure 3: The line of supercell convection at 2300 UTC 30 May shown in (right panel) observed maximum reflectivity in each column (2km grid), and (left panel) WRF model derived maximum reflectivity in each grid column (dBZ) from the BAMEX WRF forecast initialized at 0000 UTC 30 May (4km grid).

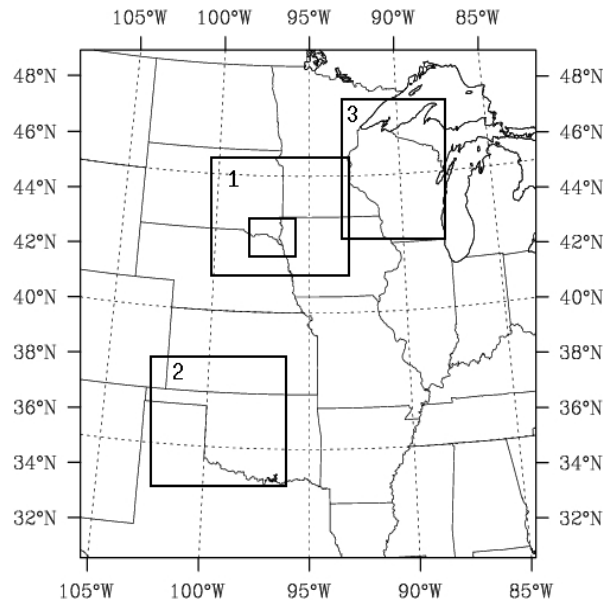


Figure 4: The parent domain and nested domains for each of the three case studies. The box inside domain 1 indicates a sub-region of the nested domain used to calculate area average quantities for case 1.

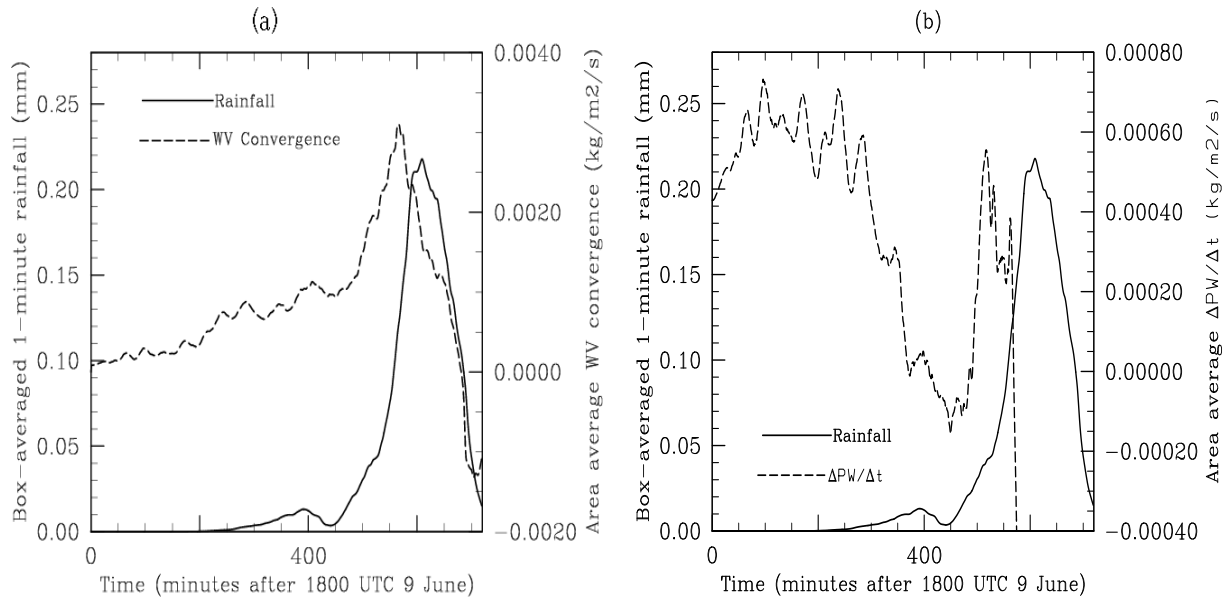


Figure 5: (a) Timeseries of 1-minute rainfall accumulation (mm, solid line) and low-level water vapor convergence ($\text{kgm}^{-2}\text{s}^{-1}$, dashed line), and (b) Timeseries of 1-minute rainfall accumulation (mm, solid line) and time rate of change of PW using $\Delta t = 1\text{min}$ ($\text{kgm}^{-2}\text{s}^{-1}$, dashed line). All quantities are area averages taken over the sub-region shown in Fig. 4.

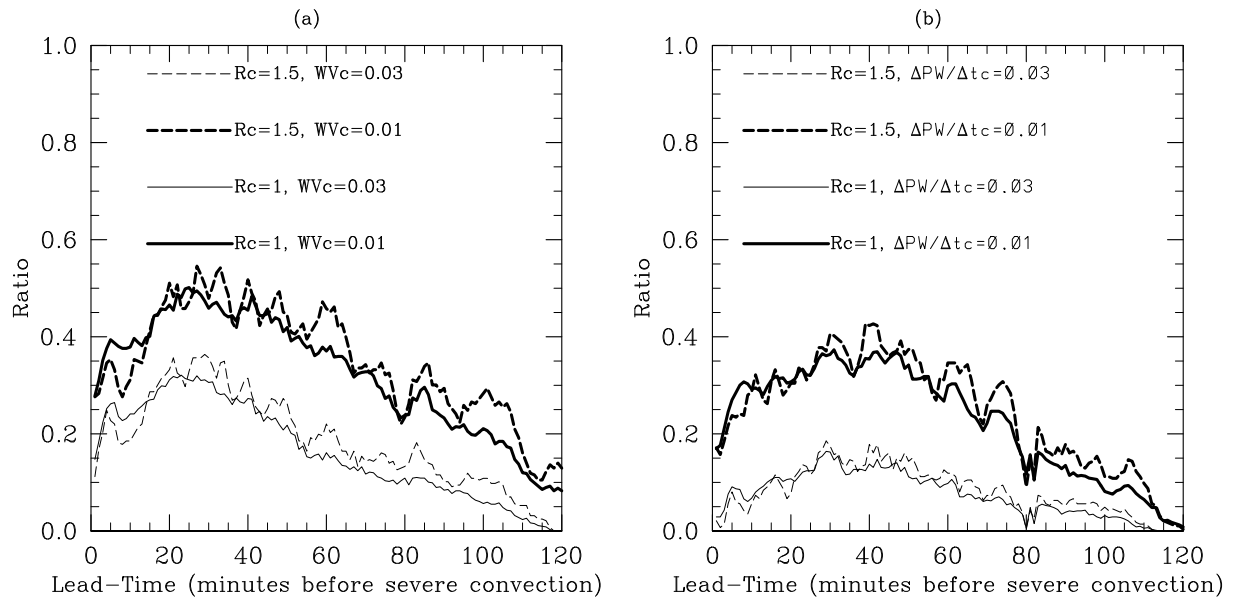


Figure 6: Ratio of the number of grid points exceeding a rainfall threshold to the number of those grid point exceeding (a) a water vapor convergence threshold and (b) a $\Delta PW/\Delta t$ threshold, for different thresholds.

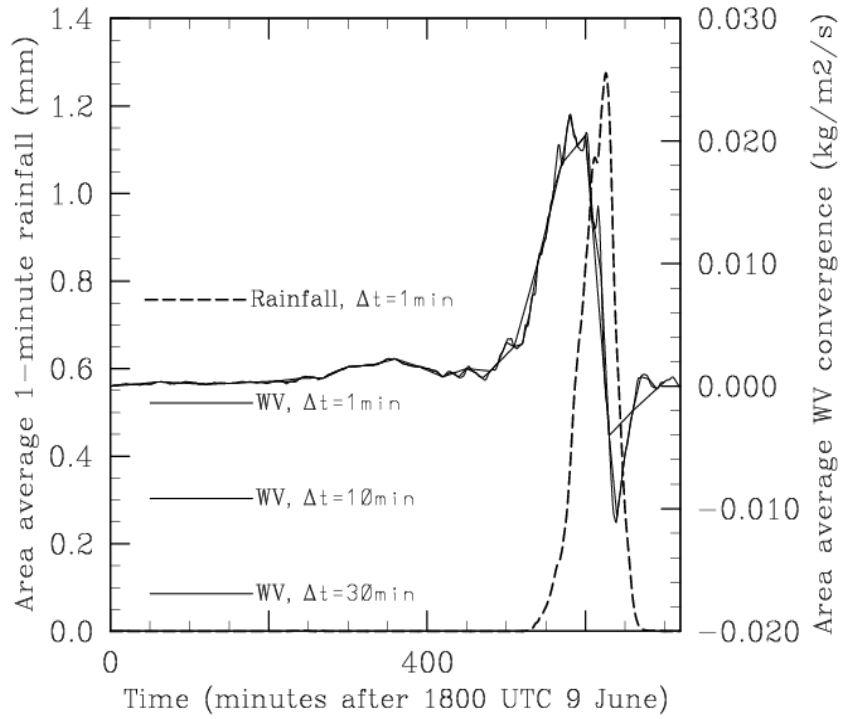


Figure 7: Timeseries of 1-minute rainfall accumulation (mm, dashed) and low-level water vapor convergence ($\text{kgm}^{-2}\text{s}^{-1}$, solid) averaged over a 31km square box using data of degraded temporal resolution.

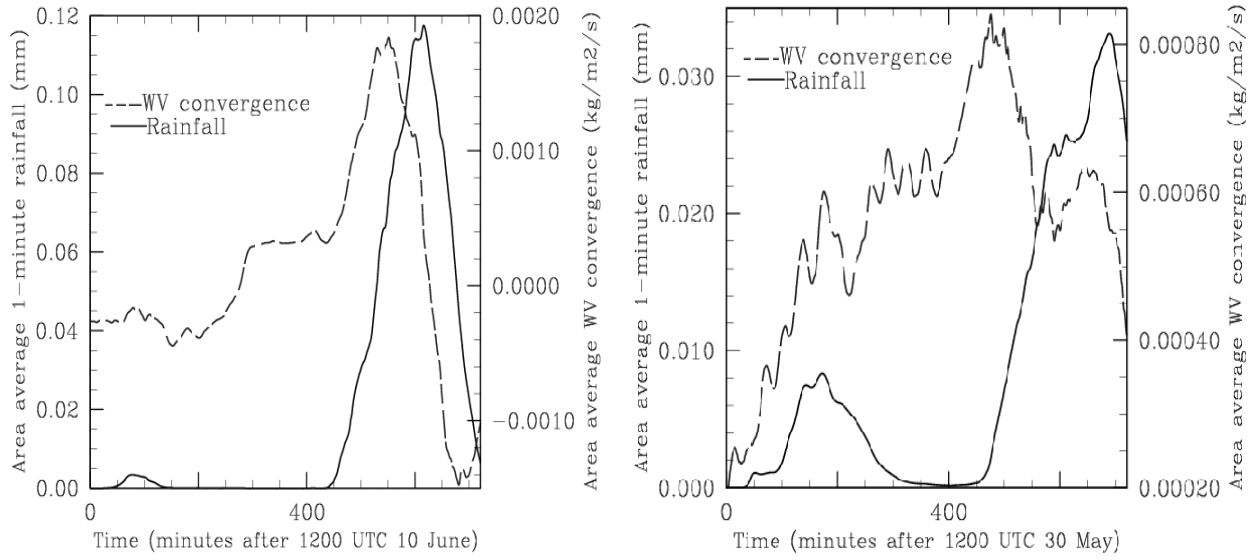


Figure 8: Timeseries of 1-minute rainfall accumulation (mm, solid line) and low-level water vapor convergence ($\text{kgm}^{-2}\text{s}^{-1}$, dashed line) averaged over a 151km square box for (left panel) case 2 and (right panel) case 3.

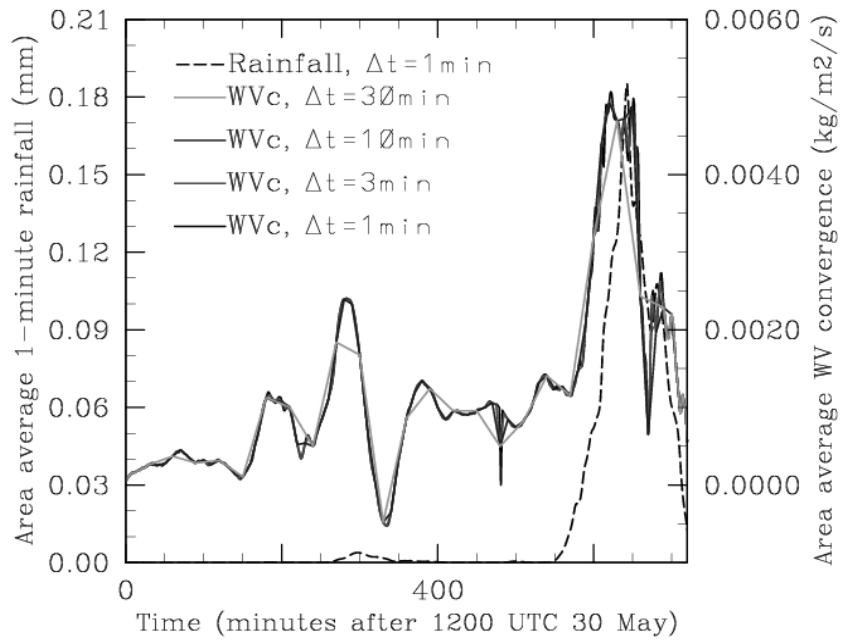


Figure 9: As for Fig. 7 but for case 2.

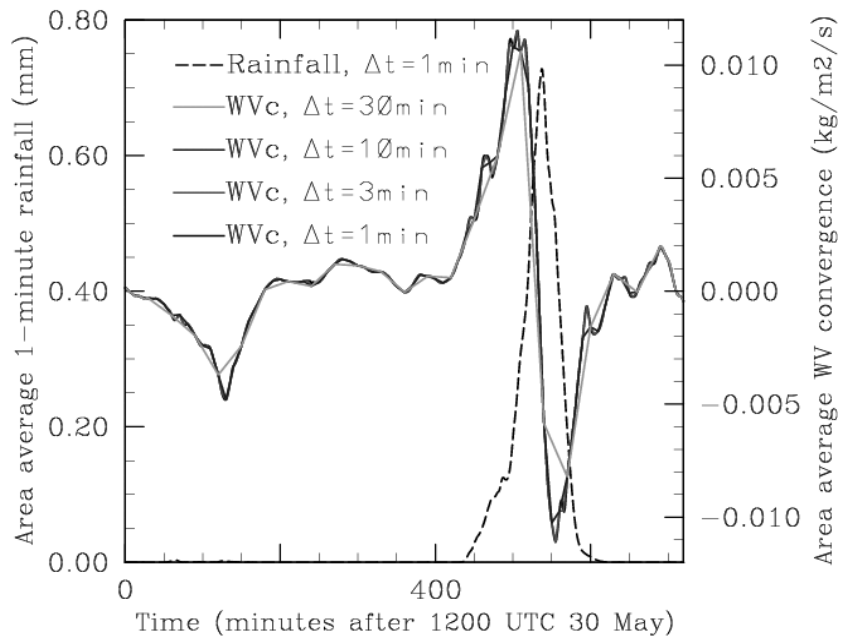


Figure 10: As for Fig. 7 but for case 3.